PCCP

ROYAL SOCIETY OF CHEMISTRY

PAPER

View Article Online
View Journal | View Issue

Cite this: *Phys. Chem. Chem. Phys.*, 2025, **27**, 6072

Synthesis of a biphenylene nanoribbon by compressing biphenylene under extreme conditions†

Zilin Zhao,[a] Guangwei Che,[a] Fang Li,[a] Yunfan Fei,[a] Hao Luo,[a] Puyi Lang,[a] Qingchao Zeng,[a] Hongcun Bai,[b] Yajie Wang,*[a] Ho-kwang Mao,[ac] Haiyan Zheng*[a] and Kuo Li*[a]

Received 8th January 2025,
Accepted 10th February 2025

DOI: 10.1039/d5cp00083a

rsc.li/pccp

Nonbenzenoid graphene nanoribbons such as biphenylene networks have gained increasing attention owing to their promising electronic and transport properties, but their scalable synthesis is still a huge challenge. Pressure-induced topochemical polymerization is an effective method to assemble molecular units into extended carbon materials, and the structure and properties of the carbon material can be tuned by modifying its molecular precursors. Herein, by directly compressing biphenylene at room temperature, we successfully synthesized crystalline biphenylene nanoribbons in milligram scale. By combining the spectroscopy and single crystal X-ray diffraction methods as well as theoretical calculation, we found that biphenylene experiences a minor phase transition above 3 GPa, and two phenyls in biphenylene undergo sequential *para*-polymerization along the *a*-axis to form a ribbon structure at 14 GPa. Our work provides an important reference for the high-pressure reaction of aromatics and the synthesis of complex nanoribbons.

Introduction

Two-dimensional materials have been interesting materials because of their advantageous physical properties.[1–4] Graphene, as one of the promising two-dimensional materials, has attracted enormous attention owing to its outstanding electronic, mechanical and optical properties.[5–7] However, it is a zero band gap semiconductor, which limits its application in digital nanoelectronic devices. Carbon nanoribbons are expected to open this band gap and therefore have potential applications in electronics and optoelectronics.[8–10] The electronic and magnetic properties of graphene nanoribbons (GNRs) can be effectively regulated by their width, edge structure, and chemical doping.[11–13] Besides, incorporating nonbenzenoid carbocyclic rings into the hexagonal aromatic carbon structure is an alternative method to modify the band gap or spin-polarized edge states. For example, the introduction of four- and eight-membered carbonic rings narrowed the band gap of zigzag GNRs and quenched its spin-polarized edge states owing to the local rehybridization of the σ and π orbitals.[14]

Biphenylene is an appealing building block for the construction of GNRs with nonbenzenoid carbon rings. The biphenylene graphene nanostructure consists of four-, six-, and eight-membered rings. Theoretical calculations suggest that the two-dimensional biphenylene graphene sheet has a metallic character, while the corresponding GNRs with armchair configuration show the opening band and the band gap decreases monotonically with an increasing width.[15] Alternatively, zig-zag configuration shows diamagnetic behavior and metallic character except for the narrowest GNRs.[15] When the width of the nanoribbon is extremely small and contains only one biphenylene unit per cell, electron mobility is high and comparable to that of 39-AGNRs (A represents armchair).[16] Furthermore, the band gap can be effectively modified by introducing chlorine or fluorine and by adjusting the degree of hydrogen saturation.[17] All of these indicate that biphenylene networks are novel carbon allotropes with tunable

[a] *Center for High Pressure Science and Technology Advanced Research, Beijing 100193, People's Republic of China. E-mail: likuo@hpstar.ac.cn, zhenghy@hpstar.ac.cn, yajie.wang@hpstar.ac.cn*
[b] *Ningxia University, Ningxia 750021, People's Republic of China*
[c] *Shanghai Advanced Research in Physical Sciences (SHARPS), Shanghai 201203, People's Republic of China*

† Electronic supplementary information (ESI) available: Assignments of infrared modes of biphenylene at 0 K and 0 GPa. (Table S1). Lattice constants for poly-BPH (0 K and 0 GPa) (Table S2). Atomic coordinates for poly-BPH (0 K and 0 GPa) (Table S3). Raman frequency shifts of biphenylene as a function of pressure (Fig. S1); infrared frequency shifts of biphenylene as a function of pressure (Fig. S2); infrared spectrum of the biphenylene recovered from different high pressures (Fig. S3); evolution of the corresponding compression ratio of lattice parameters of biphenylene (Fig. S4); the comparison of the experimental and theoretical equations of the state and lattice constants (Fig. S5); crystal structure of poly-BPH obtained using molecular dynamics (Fig. S6); high-resolution transmission electron microscopy of the product obtained from the single-crystal precursor (Fig. S7); matrix-assisted laser desorption ionization time of flight mass spectrometry of the product (Fig. S8). See DOI: **https://doi.org/10.1039/d5cp00083a**

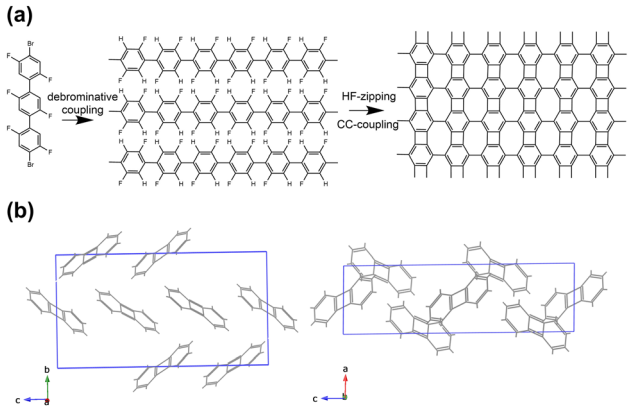

Fig. 1 (a) On-surface synthesis of biphenylene nanoribbons by Fan *et al.*[23] (b) Crystal structure of biphenylene.[26]

electronic properties and may have potential applications in the field of nano-electronic devices.

Although non-benzenoid carbocyclic rings can be produced as a defect during the preparation of carbon materials, it is still very difficult to synthesize the carbon nanostructure with repeating nonhexagonal carbon rings in a controllable manner.[18–21] Bottom-up methods, including the surface synthesis and in-solution synthesis, are common in producing biphenylene graphene nanostructures with atom-level precision. For example, by exploring the [2+2]-cycloaddition reaction, Schlütter *et al.* realized the "north-south" extension of biphenylene but failed to synthesize a biphenylene network.[22] 4,4″-Dibromo-2,2′,2″,5,5′,5″-hexafluoro-1,1′:4′,1″-terphenyl was reported to polymerize into a biphenylene network on the Au(111) surface (Fig. 1a) *via* debrominative coupling and C–C coupling using dehydrofluorination (HF-zipping).[23] However, its productivity is too low for scalable synthesis.[24] Topochemical solid-state synthesis is an effective and scalable method but is often restricted by the unpreferable arrangement of precursor molecules.[25] To date, the synthesis of biphenylene GNRs in bulk quantities is still a big challenge.

Pressure can modify intermolecular stacking and reduce the intermolecular distance directly, which has been proven as an effective method for synthesizing carbon nanoribbons from unsaturated molecules.[27–29] For example, at ≈10 GPa, 1,4-diphenyl-1,3-butadiyne (DPB) undergoes topochemical [4+2] dehydro-Diels–Alder (DDA) reactions and polymerizes into crystalline carbon nanoribbons with a width of approximately 13 Å.[30] 1,3,5-Triethynylbenzene (TEB) also polymerizes into carbon nanoribbons *via* a DDA reaction at 4 GPa.[31] Azobenzene polymerizes *via* two distinct routes in the crystal to form a van der Waals heteronanoribbon.[32] These reactions follow the principle of topochemical polymerization, allowing us to predict products based on the structures of reactants and synthesize carbon nanoribbons with atom-level precision.[33] Based on this principle, we investigated biphenylene as a precursor for the synthesis of biphenylene nanoribbons under high pressure. As shown in Fig. 1b, biphenylene molecules are stacked in a herringbone arrangement–like benzene.[26,34] Under high pressure, biphenylene was predicted to undergo anisotropic compression, resulting in a decrease in the band gap.[35] In this work, we synthesized an sp^3C(H)-substituted biphenylene nanoribbon in bulk phase under high pressure at room temperature. We discovered that biphenylene undergoes a minor phase transition at 3 GPa and an irreversible reaction at 14 GPa. Based on computational and experimental results, we proposed a nanoribbon model for the product. This nanoribbon contains sp^3C(H), different from known nonbenzenoid graphene nanoribbons, which may have different electronic properties.[17] Our work provides a potential route to synthesize nanoribbons of uncommon topologies, including those with four-membered and eight-membered rings.

Experimental

Biphenylene (99.9%) was purchased from Innochem and used without further purification. For Raman and infrared (IR) experiments, biphenylene powder was gently ground in an agate mortar for over 10 minutes. For single crystal X-ray diffraction (XRD) and ultraviolet-visible (UV-vis) spectroscopy experiments, a biphenylene single crystal was obtained through recrystallization from methanol. The symmetric diamond anvil cell (DAC) with an anvil culet diameter of 300 μm was used to generate high pressure. Type-IIa diamond anvils were used for infrared experiments to avoid absorption bands at 1300–1000 cm^{-1}. T-301 stainless steel gaskets were pre-indented to a thickness of about 30 μm, and central holes with a diameter of 150 μm were drilled to serve as a sample chamber. The pressure was determined by measuring ruby fluorescence according to the equation P (GPa) = $248.4[(\lambda/\lambda_0)^{7.665} - 1]$.[36] Raman experiments were conducted using a Renishaw Raman microscope with an excitation laser wavelength of 532 nm. The system was calibrated using the Si line. Infrared experiments were performed on Bruker VERTEX 70v with a HYPERION 2000 microscope. A Globar was used as a conventional source. The spectra were collected in the transmission mode in the 600–4000 cm^{-1} range with a resolution of 4 cm^{-1}. No pressure medium was used in IR and Raman experiments. UV-vis absorption experiments were collected in a home-designed spectroscopy system (built by Ideaoptics) in the microregion with a xenon light source from 200 to 1000 nm. Silicone oil was used as the pressure-transmitting medium for the UV-vis experiment. Single-crystal X-ray diffraction data were collected using Rigaku XtaLAB Synergy Custom with Mo K_α radiation. The CrysAlis program was used for data collection. The pressure-transmitting medium was helium.

Paris-Edinburgh (PE) Press VX3 was used to synthesize a biphenylene polymeric product (PE25) under 25 GPa, and sintered diamond double toroidal anvils with 3 mm dimple diameters were utilized for the experiments. Stainless steel gaskets were explored as the sample chamber. An automatic hydraulic oil syringe pump drove the system, and the pressure was estimated from the PLANET group calibration curve.[37] The powder (no pressure transmitting medium) and single crystal samples (pressure transmitting medium is methanol : ethanol : water = 16 : 3 : 1) were loaded into the PE press, and the oil pressure was quickly increased to 200 bar (about 2 GPa) to seal the sample. Next, the

sample was compressed to a high pressure of 25 GPa (oil pressure of about 1200 bar) and kept under the target pressure for about 10 hours. The rates of compression and decompression were 6 bar min^{-1} (200–400 bar), 4 bar min^{-1} (400–600 bar), 1 bar min^{-1} (600–1000 bar), and 0.5 bar min^{-1} (1000–1200 bar). After releasing the pressure, unreacted biphenylene was removed from PE25 by washing with dichloromethane, and a yellow sample (poly-biphenylene) was finally obtained.

Matrix-assisted laser desorption ionization time of flight mass spectrometry (MALDI-TOF-MS) was recorded on AB Sciex 5800 for PE25. Samples were dissolved in dichloromethane and mixed with matrix solution (dichloromethane and *trans*-2-[3-(4-*tert*-butylphenyl)-2-methyl-2-propenylidene] malononitrile (DCTB)). Measurement was taken using the reflector mode in the 100–8000 *m*/*z* range.

Powder X-ray diffraction data were recorded on a PANalytical Empyrean diffractometer with mono-chromatized Cu K_α radiation from 5° to 65°. Transmission electron microscopy (TEM) images were recorded on JEM-2100 under a bias voltage of 200 kV. A scanning electron microscopy (SEM) image was recorded on a JEOL JSM-7900F field-emission scanning electron microscope operated at 3 kV.

The structure optimization, Raman spectra, infrared spectra, band gap of biphenylene and the product model were obtained by employing density functional theory (DFT) calculations within the generalized gradient approximation (GGA) implemented in the CASTEP module.[38–40] The energy convergence criterion of structure optimization is 5.0e-6 eV per atom, the residual force for inter-atomic interactions is 0.01 eV $Å^{-1}$, and the residual stress in lattices is 0.02 GPa. The Raman and infrared modes were calculated using norm-conserving pseudopotentials with an energy cutoff for the plane-wave basis set at 720 eV and *k*-point sampling $<0.05 \times 2\pi$ $Å^{-1}$.[41,42] Molecular dynamics simulation was performed using the Vienna Ab initio Simulation Package (VASP).[43] We constructed a supercell consisting of a $2a \times 2b \times 1c$ unit cell. The simulation was conducted at 300 K. Each step took 0.5 fs, and a total of 10000 steps were performed.

Results and discussion

Raman spectra of biphenylene under high pressure

In situ, the Raman spectrum of biphenylene under high pressure was collected to first check its phase transitions, as shown in Fig. 2. The assignment of Raman peaks, as shown in the figure, was achieved through theoretical calculation. Under compression, all the vibrational modes blue shifted gradually. At a pressure of 3.0–4.6 GPa, two new lattice modes emerged at 74 and 90 cm^{-1}, and a new peak corresponding to =CH stretching vibration (ν_{CH}) emerged at 3000–3100 cm^{-1}. Pressure-dependent Raman shifts are summarized in Fig. S1 (ESI†), where discontinuity can be clearly observed, confirming the phase transition. Above 13 GPa, the intensity of the signal exceeded the detector's range owing to the enhanced fluorescence background, indicating the occurrence of chemical transformation or defects in the crystal.[44] Combining the infrared spectra and single crystal XRD

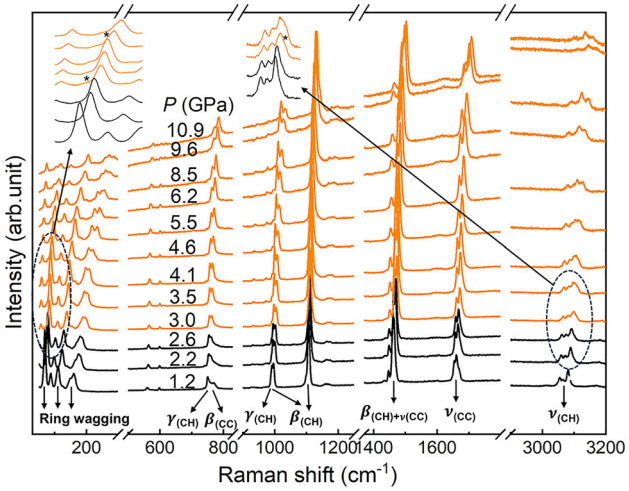

Fig. 2 Raman spectra of powder biphenylene under non-hydrostatic pressure conditions. New peaks after phase transitions are marked by asterisks. γ represents out-of-plane bending vibration; ν represents stretching vibration; β stands for in-plane bending vibration.

results described below, a minor transition from phase I to II was established with a boundary at 3 GPa.

Mid-IR spectra of biphenylene under high pressure

In situ, the IR spectra of biphenylene were measured up to 30 GPa under non-hydrostatic pressure conditions to investigate the reaction process (Fig. 3). The assignment of the IR modes of biphenylene is shown in Table S1 (ESI†), based on the calculation at 0 GPa. Above 3.6 GPa, a new peak appears on the high-frequency side of CH out-of-plane bending vibration ($\gamma_{(CH)}$, 943 cm^{-1}), and a new peak at 773 cm^{-1} is detected, corresponding to the transition from phase I to II. Additionally, a shoulder band

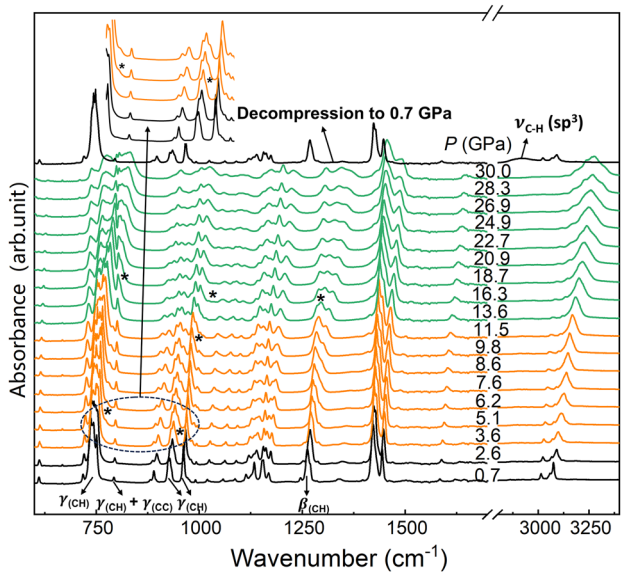

Fig. 3 IR spectra of biphenylene powder under non-hydrostatic pressure conditions. New peaks after phase transitions are marked by asterisks. γ represents out-of-plane bending vibration; β stands for in-plane bending vibration.

around 987 cm^{-1} is observed on the high-frequency side of the CH out-of-plane bending vibration ($\gamma_{(CH)}$) at 9.8 GPa, indicating a sluggish phase transition. Around 14 GPa, the CH in-plane bending vibration ($\beta_{(CH)}$, 1288 cm^{-1}) splits. Two new peaks emerged at 808 and 1035 cm^{-1}. Upon further compression, the peak broadens, and the dependence of the modes on pressure exhibits a clear discontinuity (Fig. S2, ESI†). As discussed later, this is the onset of the reaction. After maintaining biphenylene at 30 GPa for 17 hours and subsequently decompressing it to 0.7 GPa, an orange sample with a new broad peak at 2914 cm^{-1} was observed, which is recognized as sp^3-C–H stretching ($\nu_{CH}(sp^3)$) and therefore demonstrates irreversible pressure-induced polymerization. To determine the reaction pressure, we compressed biphenylene to different maximum pressures and measured the IR spectra of recovered samples. sp^3-C can only be obtained above 14.7 GPa, and the reaction pressure was therefore determined to be 14.7 GPa (Fig. S3, ESI†).

Structure analysis of biphenylene under high pressure

The crystal structure is crucial for understanding phase transitions and reactions. We performed *in situ* single-crystal X-ray diffraction measurements to investigate its structural evolution under compression. Fig. 4a shows the pressure dependence of lattice constants. During compression, biphenylene shows an obvious anisotropic compression, where the *a* and *b* axes have a similar compression ratio, which is greater than that of the *c* axis (Fig. S4, ESI†). At 25 GPa, the compression ratios for the *a*-axis, *b*-axis, and *c*-axis are 85.6%, 84.4%, and 90.1%, respectively, indicating that the possible bonding directions are along the *a* or *b* axes, which is consistent with the optical observation shown in Fig. 5a.[45–47] Additionally, a discontinuity of lattice constants is observed at 3.8 GPa, corresponding to the phase I-to-II transition observed in spectroscopy results, but with the unit cell volume scarcely affected. At 14.3 GPa, discontinuities of both the lattice constants and unit cell volume were clearly observed in Fig. 4a and b, indicating the occurrence of the reaction. DFT simulation data also support these experimental results (Fig. S5, ESI†). As shown in Fig. 4b, we fit the pressure–volume curve utilizing the 3rd order Birch–Murnaghan equation of state (B-M EOS):

$$P(V) = \frac{3}{2}B_0\left[\left(\frac{V_0}{V}\right)^{\frac{7}{3}} - \left(\frac{V_0}{V}\right)^{\frac{5}{3}}\right] \times \left\{1 + \frac{3}{4}(B_1 - 4)\left[\left(\frac{V_0}{V}\right)^{\frac{2}{3}} - 1\right]\right\},$$

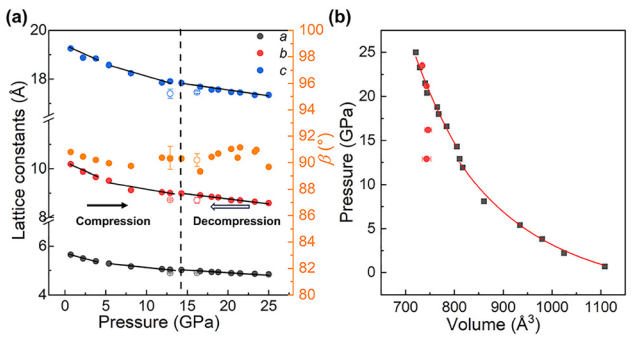

Fig. 4 *In situ* single crystal XRD investigations of biphenylene under hydrostatic pressure conditions. (a) Lattice parameters during compression (solid circles) and decompression (hollow circles). (b) Pressure dependence of the unit cell volume of biphenylene during compression (black square) and decompression (red circle). The solid lines represent the fitting results of the 3rd order B–M EOS in the pressure range of 0.9–25.0 GPa. Before the reaction, the error of the cell parameters is smaller than the symbol.

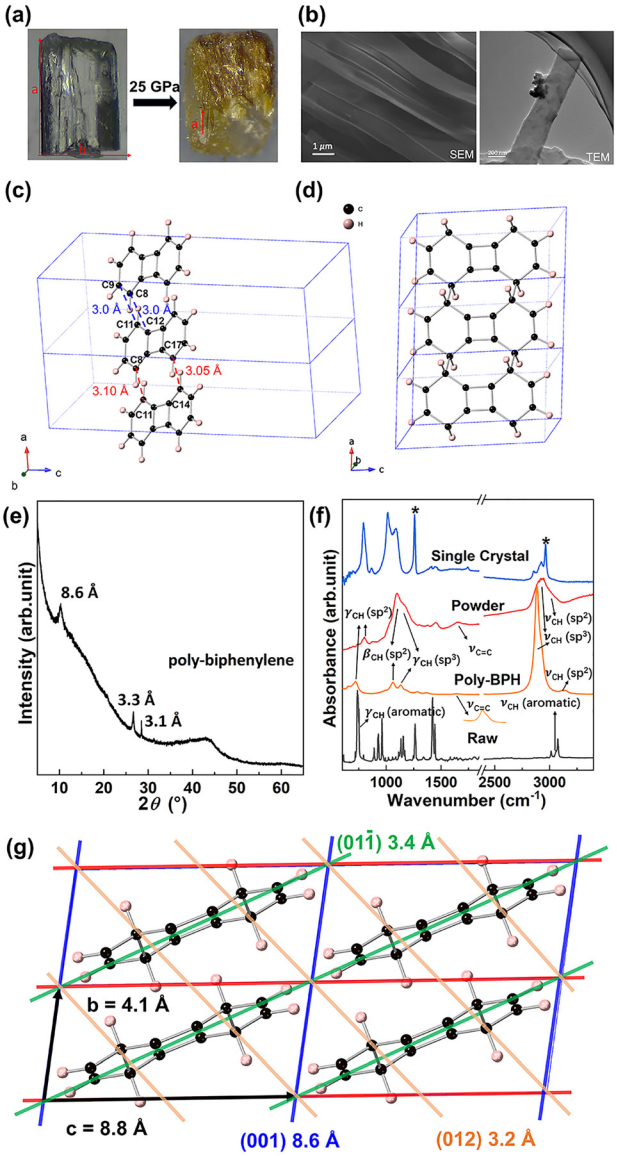

Fig. 5 Structural investigation and simulation of the polymeric product. (a) Optical and (b) SEM and TEM images of poly-biphenylene. (c) Crystal structure of biphenylene at 12.9 GPa obtained through DFT calculations. (d) Structure of poly-BPH optimized through DFT calculations. (e) Powder XRD spectra of poly-biphenylene. (f) IR spectra of the raw material, powder and single crystal poly-biphenylene, and poly-BPH calculated using DFT. Peak shapes of poly-BPH were modeled using a Lorentzian function with a full width at half-maximum of 50 cm^{-1}.[50] The asterisked peaks at 1258 and 2963 cm^{-1} correspond to residual dichloromethane. γ represents out-of-plane bending vibration; ν represents stretching vibration; β stands for in-plane bending vibration. (g) The structure of poly-BPH viewed along the *a*-axis using DFT calculation.

where V_0 is the unit cell volume under ambient conditions, while B_0 and B_1 are ambient bulk modulus and its derivative, respectively. Two curves were needed to fit the data. Below 14.3 GPa, the V_0 is 1164 ± 41 Å^3, which is consistent with the experimental unit cell volume at ambient pressure.[48,49] B_0 and B_1 values are 15 ± 6 GPa and 4.7 ± 1.5, respectively. In the pressure range of 14.3–25 GPa, V_0 = 1079 ± 31 Å^3, B_0 = 27 ± 4 GPa, and B_1 is fixed at 4. The transition pressure is consistent with the reaction pressure observed in the IR spectrum. The lattice parameters of the monomer can still be obtained up to 25 GPa. During decompression, the cell volume and lattice parameters were almost unchanged. Until decompression to ≈13 GPa, all diffraction points suddenly disappeared, indicating that the reaction may have taken place during decompression, enough spaces are necessary for the reaction to proceed, and extra applied pressure suppressed the reaction. Combining these findings with the IR results, we can conclude that biphenylene experienced a minor phase transition above 3 GPa, with minimal effects on the lattice, and an irreversible chemical reaction above 14 GPa.

Product and the reaction mechanism

To understand the structure of the product, we synthesized a biphenylene polymeric product (PE-25) starting from powder and single crystal precursors using the PE press at 25 GPa under non-hydrostatic and hydrostatic pressure conditions. After decompression to ambient pressure, unreacted biphenylene was removed using dichloromethane, and a yellow sample (poly-biphenylene) was finally obtained. Before synthesizing with the PE press, we determined the orientation of the biphenylene single crystal by employing single crystal XRD. Fig. 5a shows the optical images of the crystal before and after the reaction. The recovered product was yellowish with the ribbon structure extended along the *a*-axis, which was confirmed by the SEM and TEM results (Fig. 5b).

Based on the experimental cell parameters determined through single crystal XRD, we optimized the critical crystal structure of biphenylene at 12.9 GPa *via* DFT calculations to identify short C···C contacts, which can form a new C–C bond according to the topochemical reaction rule.[51–54] As shown in Fig. 5c, biphenylene molecules remain slip-stacked along the *a*-axis, and there are two types of short C···C distances. One is the C···C distance between C9···C11 and C8···C12. They have equivalent C···C contacts with a distance of 3.0 Å, which is close to the critical distance range of the polymerization of aromatics (2.8–3.0 Å).[33,55–61] This suggests they may simultaneously form two C–C bonds through the [2+2] cycloaddition reaction. However, this reaction is symmetry-forbidden and usually has a high energy barrier. Another short C···C distance between C8···C11 (3.10 Å) was also observed, which can initiate the 1,4-addition polymerization (*para*-polymerization) reaction along the *a*-axis. This reaction is also a possible reaction type observed in the aromatic compounds under high pressure and consistent with the reaction direction observed for the polymeric product from the single crystal monomer, which suggests that the 1,4-addition polymerization reaction is a more plausible reaction route.[62] Based on this, we proposed a structure model poly-BPH for the product and optimized it using DFT at ambient pressure, as shown in Fig. 5d and Tables S2 and S3 (ESI†). The molecular dynamics of poly-BPH indicate that the structure is stable at ambient pressure (Fig. S6, ESI†).

This model was evidenced by the XRD data of poly-biphenylene. XRD data show a featured peak at 8.6 Å (Fig. 5e), which fits well with the lattice stripes in the high-resolution transmission electron microscopy of the products (Fig. S7, ESI†). This corresponds to the (001) plane of poly-BPH (Fig. 5g), approximately the width of the nanoribbons. XRD peaks at 3.3 Å and 3.1 Å are not characteristic but can still be indexed by the poly-BPH model.

Fig. 5f presents the experimental IR spectrum of poly-biphenylene and its simulated data. The IR spectra of poly-biphenylene starting from the single crystal and powder precursor are almost identical, with the former having much sharper peaks, indicating better crystallinity. Compared with the IR spectra of biphenylene, the CH out-of-plane bending vibration (γ_{CH}) of the phenyl moieties degraded and the C=C bonds ($\nu_{C=C}$, 1600 cm^{-1}) became stronger, indicating that aromaticity is destroyed and an isolated double bond is formed. Moreover, we found a new peak ($\nu_{CH}(sp^3)$) corresponding to sp^{3}CH at about 2900 cm^{-1}, while the intensity of the sp^{2}CH peak ($\nu_{CH}(sp^2)$) decreased. This observation suggests that part of the carbon on the benzene ring has been converted into saturated carbon. We simulated the IR spectrum of the poly-BPH model using DFT, which shows good agreement with the experimental results, with only a minor shift.

MALDI-TOF-MS shows that the peaks of PE25 without elimination of small molecules are dominating, such as $(C_{12}H_8)_2$ (Fig. S8, ESI†). This indicates that addition polymerization instead of condensation polymerization is the main reaction path and is consistent with our model.

According to the above experimental and computational results, biphenylene under high pressure likely undergoes 1,4-addition polymerization to form nanoribbons, resulting in a poly-BPH structure.

Electronic structure and properties

We also studied the electronic structure of biphenylene and the polymerized product by collecting *in situ* UV-visible absorption spectra and DFT calculations (Fig. 6a and b). Biphenylene exhibits two absorptions, both of which gradually get red shifted with increasing pressure and merge above 3.1 GPa, where the phase transition occurs. Above 12.3 GPa, a change in the shift rate was clearly observed in Fig. 6a, suggesting a reaction consistent with other experimental results. The decrease in the experimental band gap is qualitatively consistent with the theoretical calculation (Fig. 6b). The recovered product demonstrates an optical band gap of 1.74 eV (Fig. 6c), much smaller than that of biphenylene (>2.98 eV, Fig. 6b). We also simulated the band structure of the poly-BPH model (Fig. 6d), and the obtained band gap is 0.86 eV. The difference between the experimental and calculated band gap is due to the underestimation of the band gap when using GGA-PBE.

Conclusions

In conclusion, the structural evolution of biphenylene was investigated under extremely high pressure and ambient temperature

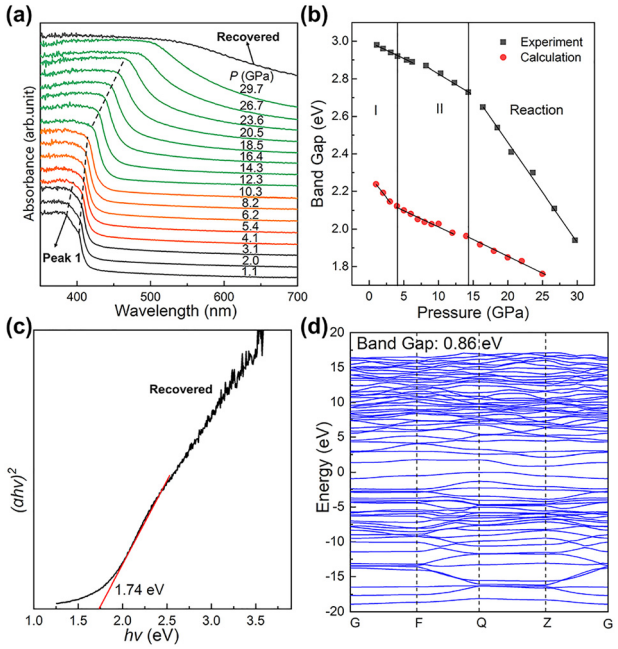

Fig. 6 The band gap of biphenylene and poly-BPH. (a) *In situ* UV-vis spectra of biphenylene under hydrostatic pressure conditions. (b) Variations in the band gap as a function of pressure. The black squares represent experimental results, and the red circles represent calculation results. The solid line represents the boundaries of different phases. (c) Tauc plot to determine the optical band gap of the recovered product, with extrapolation of the linear region estimating approximately 1.74 eV. (d) The calculated band structure of the poly-BPH model.

using *in situ* Raman, mid-IR spectroscopy, X-ray diffraction, *etc.* A phase transition was identified above 3 GPa. Phase II undergoes irreversible polymerization above 14 GPa, resulting in a crystalline biphenylene nanoribbon. By combining experimental and computational results, we suggest that biphenylene may undergo 1,4-addition along the *a*-axis at high pressure and propose a biphenylene nanoribbon model with sp^3C(H), which is quite different from the known biphenylene network. Our work demonstrates the pressure-induced polymerization of biphenylene and provides essential information for understanding the polymerization of biphenylene. This work also provides an important reference for high pressure synthesis of nanoribbons with non-benzenoid rings.

Author contributions

Z. Zhao performed the experiments and theoretical calculations and wrote the original draft. F. Li and Q. Zeng helped collect the XRD data. G. Che, Y. Fei and H. Luo helped collect the TEM data. P. Lang and H. Bai helped complete the theoretical calculations. H. Zheng, Y. Wang and K. Li led the entire experiment, data analysis, and manuscript writing. H. K. Mao led funding acquisition. All the authors approved the final version of the manuscript.

Data availability

The data supporting this article have been included as part of the ESI.†

Conflicts of interest

There are no conflicts to declare.

Acknowledgements

The authors acknowledge the support of the National Key Research and Development Program of China (No. 2023YFA1406200 and 2019YFA0708502) and National Natural Science Foundation of China (Grant No.: 22022101). The authors acknowledge the support of Synergetic Extreme Condition User Facility (SECUF) (PT-001578).

Notes and references

1 Z. Li, J. Han, S. Cao, Z. Zhang and X. Deng, *Phys. Rev. B*, 2023, **108**, 184413.
2 Z. Li, J. Han, S. Cao, Z. Zhang and X. Deng, *Phys. Rev. Appl.*, 2024, **21**, 054062.
3 V. Shanmugam, R. Mensah, K. Babu, S. Gawusu, A. Chanda, Y. Tu, R. Neisiany, M. Försth, G. Sas and O. Das, *Part. Part. Syst. Charact.*, 2022, **39**, 2200031.
4 Y. Yi, Z. Li, S. Cao, J. Han and Z. Zhang, *Appl. Surf. Sci.*, 2025, **682**, 161730.
5 K. S. Novoselov, A. K. Geim, S. V. Morozov, D. Jiang, Y. Zhang, S. V. Dubonos, I. V. Grigorieva and A. A. Firsov, *Science*, 2004, **306**, 666–669.
6 A. K. Geim and K. S. Novoselov, *Nat. Mater.*, 2007, **6**, 183–191.
7 P. Blake, P. D. Brimicombe, R. R. Nair, T. J. Booth, D. Jiang, F. Schedin, L. A. Ponomarenko, S. V. Morozov, H. F. Gleeson, E. W. Hill, A. K. Geim and K. S. Novoselov, *Nano Lett.*, 2008, **8**, 1704–1708.
8 F. Kang, L. Sun, W. Gao, Q. Sun and W. Xu, *ACS Nano*, 2023, **17**, 8717–8722.
9 Z. Chen, A. Narita and K. Müllen, *Adv. Mater.*, 2020, **32**, e2001893.
10 S. Wang and J. Wang, *J. Phys. Chem. C*, 2012, **116**, 10193–10197.
11 R. S. K. Houtsma, J. de la Rie and M. Stöhr, *Chem. Soc. Rev.*, 2021, **50**, 6541–6568.
12 M. Fujita, K. Wakabayashi, K. Nakada and K. Kusakabe, *J. Phys. Soc. Jpn.*, 1996, **65**, 1920–1923.
13 P. Ruffieux, J. Cai, N. C. Plumb, L. Patthey, D. Prezzi, A. Ferretti, E. Molinari, X. Feng, K. Müllen, C. A. Pignedoli and R. Fasel, *ACS Nano*, 2012, **6**, 6930–6935.
14 M. Liu, M. Liu, L. She, Z. Zha, J. Pan, S. Li, T. Li, Y. He, Z. Cai, J. Wang, Y. Zheng, X. Qiu and D. Zhong, *Nat. Commun.*, 2017, **8**, 14924.
15 M. A. Hudspeth, B. W. Whitman, V. Barone and J. E. Peralta, *ACS Nano*, 2010, **4**, 4565–4570.
16 H. Ge, G. Wang and Y. Liao, *Chem. Phys. Lett.*, 2016, **648**, 97–101.
17 P. A. Denis, *J. Phys. Chem. C*, 2014, **118**, 24976–24982.
18 C. Ma, H. Sun, Y. Zhao, B. Li, Q. Li, A. Zhao, X. Wang, Y. Luo, J. Yang, B. Wang and J. G. Hou, *Phys. Rev. Lett.*, 2014, **112**, 226802.
19 J. Kotakoski, A. V. Krasheninnikov, U. Kaiser and J. C. Meyer, *Phys. Rev. Lett.*, 2011, **106**, 105505.

20 T. Dienel, S. Kawai, H. Söde, X. Feng, K. Müllen, P. Ruffieux, R. Fasel and O. Gröning, *Nano Lett.*, 2015, **15**, 5185–5190.
21 A. Lahiri, Y. Lin, P. Bozkurt, I. I. Oleynik and M. Batzill, *Nat. Nanotechnol.*, 2010, **5**, 326–329.
22 F. Schlütter, T. Nishiuchi, V. Enkelmann and K. Müllen, *Angew. Chem., Int. Ed.*, 2014, **53**, 1538–1542.
23 Q. Fan, L. Yan, M. W. Tripp, O. Krejčí, S. Dimosthenous, S. R. Kachel, M. Chen, A. S. Foster, U. Koert, P. Liljeroth and J. M. Gottfried, *Science*, 2021, **372**, 852–856.
24 A. Narita, X. Feng and K. Müllen, *Chem. Rec.*, 2015, **15**, 295–309.
25 Y. Yano, N. Mitoma, H. Ito and K. Itami, *J. Org. Chem.*, 2020, **85**, 4–33.
26 R. Boese, D. Bläser and R. Latz, *Acta Crystallogr. C*, 1999, **55**, IUC9900067.
27 Y. Fei, K. Li and H. Zheng, *Chin. J. High Pressure Phys.*, 2023, **37**, 060101.
28 W. Zhao, J. Zhang, Z. Sun, G. Xiao, H. Zheng, K. Li, M. Li and B. Zou, *CCS Chem.*, 2025, DOI: 10.31635/ccschem.025.202405293.
29 R. Bini, M. Ceppatelli, M. Citroni and V. Schettino, *Chem. Phys.*, 2012, **398**, 262–268.
30 P. Zhang, X. Tang, Y. Wang, X. Wang, D. Gao, Y. Li, H. Zheng, Y. Wang, X. Wang, R. Fu, M. Tang, K. Ikeda, P. Miao, T. Hattori, A. Sano-Furukawa, C. A. Tulk, J. J. Molaison, X. Dong, K. Li, J. Ju and H. K. Mao, *J. Am. Chem. Soc.*, 2020, **142**, 17662–17669.
31 Y. Li, X. Tang, P. Zhang, Y. Wang, X. Yang, X. Wang, K. Li, Y. Wang, N. Wu, M. Tang, J. Xiang, X. Lin, H. H. Lee, X. Dong, H. Zheng and H. K. Mao, *J. Phys. Chem. Lett.*, 2021, **12**, 7140–7145.
32 P. Zhang, D. Gao, X. Tang, X. Yang, H. Zheng, Y. Wang, X. Wang, J. Xu, Z. Wang, J. Liu, X. Wang, J. Ju, M. Tang, X. Dong, K. Li and H. K. Mao, *J. Am. Chem. Soc.*, 2023, **145**, 6845–6852.
33 X. Tang, X. Dong, C. Zhang, K. Li, H. Zheng and H. K. Mao, *Matter. Radiat. Extremes*, 2023, **8**, 058402.
34 J. Lüder, M. de Simone, R. Totani, M. Coreno, C. Grazioli, B. Sanyal, O. Eriksson, B. Brena and C. Puglia, *J. Chem. Phys.*, 2015, **142**, 074305.
35 Q. Wang and Q. Zhou, *Mol. Simulat.*, 2020, **46**, 987–993.
36 H. K. Mao, J. Xu and P. M. Bell, *Res-Sol. Ea.*, 2012, **91**, 4673–4676.
37 T. Hattori, A. Sano-Furukawa, S. Machida, J. Abe, K. Funakoshi, H. Arima and N. Okazaki, *High Pressure Res.*, 2019, **39**, 417–425.
38 J. P. Perdew, J. A. Chevary, S. H. Vosko, K. A. Jackson, M. R. Pederson, D. J. Singh and C. Fiolhais, *Phys. Rev. B*, 1992, **46**, 6671–6687.
39 S. J. Clark, M. D. Segall, C. J. Pickard, P. J. Hasnip, M. I. J. Probert, K. Refson and M. C. Payne, *Z. Kristallogr. – Cryst. Mater.*, 2005, **220**, 567–570.
40 Y. M. Juan, E. Kaxiras and R. G. Gordon, *Phys. Rev. B*, 1995, **51**, 9521.
41 S. Baroni, S. D. Gironcoli, A. D. Corso and P. Giannozzi, *Rev. Mod. Phys.*, 2001, **73**, 515–562.
42 D. Porezag and M. R. Pederson, *Phys. Rev. B*, 1996, **54**, 7830–7836.
43 G. Kresse and J. Furthmüller, *Comput. Mater. Sci.*, 1996, **6**, 15–50.
44 A. Biswas, M. D. Ward, T. Wang, L. Zhu, H. T. Huang, J. V. Badding, V. H. Crespi and T. A. Strobel, *J. Phys. Chem. Lett.*, 2019, **10**, 7164–7171.
45 S. Dunning, B. Chen, L. Zhu, G. Cody, S. Chariton, V. Parkapenka, D. Zhang and T. Strobel, *Angew. Chem., Int. Ed.*, 2023, **62**, e202217023.
46 G. Che, Y. Fei, X. Tang, Z. Zhao, T. Hattori, J. Abe, X. Wang, J. Ju, X. Dong, Y. Wang, K. Li and H. Zheng, *Phys. Chem. Chem. Phys.*, 2025, **27**, 1112–1118.
47 X. Wang, X. Yang, Y. Wang, X. Tang, H. Zheng, P. Zhang, D. Gao, G. Che, Z. Wang, A. Guan, J. F. Xiang, M. Tang, X. Dong, K. Li and H. K. Mao, *J. Am. Chem. Soc.*, 2022, **144**, 21837–21842.
48 T. C. W. Mak and J. Trotter, *J. Chem. Soc.*, 1962, 1–8.
49 J. K. Fawcett and J. Trotter, *Acta. Crystallogr.*, 1966, **20**, 87–93.
50 T. Lu and F. Chen, *J. Comput. Chem.*, 2012, **33**, 580–592.
51 H. Kuntrapakam, R. Arthi, R. Cijil, R. P. Javed, R. Rishika and M. S. Kana, *Chem. Soc. Rev.*, 2021, **50**, 4062–4099.
52 B. Kumar and S. Ramkinkar, *Chem. Soc. Rev.*, 2013, **42**, 950–967.
53 G. M. J. Schmidt, *Pure Appl. Chem.*, 1971, **27**, 647–678.
54 K. Hema and K. M. Sureshan, *Acc. Chem. Res.*, 2019, **52**, 3149–3163.
55 F. Li, J. Xu, H. Zheng and K. Li, *Molecules*, 2021, **26**, 7581.
56 J. Sun, X. Dong, Y. Wang, K. Li, H. Zheng, L. Wang, G. D. Cody, C. A. Tulk, J. J. Molaison, X. Lin, Y. Meng, C. Jin and H. K. Mao, *Angew. Chem., Int. Ed.*, 2017, **56**, 6553–6557.
57 G. Qi, S. Song, Z. Deng, D. Huang, F. Chen, B. Yan, H. Gou, Q. Zhang and Y. Wang, *CCS Chem.*, 2023, **5**, 1815–1826.
58 X. Wang, X. Tang, P. Zhang, Y. Wang, D. Gao, J. Liu, K. Hui, Y. Wang, X. Dong, T. Hattori, A. Sano-Furukawa, K. Ikeda, P. Miao, X. Lin, M. Tang, Z. Zuo, H. Zheng, K. Li and H. K. Mao, *J. Phys. Chem. Lett.*, 2021, **12**, 12055–12061.
59 L. Ciabini, M. Santoro, F. A. Gorelli, R. Bini, V. Schettino and S. Raugei, *Nat. Mater.*, 2007, **6**, 39–43.
60 T. C. Fitzgibbons, M. Guthrie, E. S. Xu, V. H. Crespi, S. K. Davidowski, G. D. Cody, N. Alem and J. V. Badding, *Nat. Mater.*, 2015, **14**, 43–47.
61 Y. Wang, X. Dong, X. Tang, H. Zheng, K. Li, X. Lin, L. Fang, G. Sun, X. Chen, L. Xie, C. L. Bull, N. P. Funnell, T. Hattori, A. Sano- Furukawa, J. Chen, D. K. Hensley, G. D. Cody, Y. Ren, H. H. Lee and H. K. Mao, *Angew. Chem., Int. Ed.*, 2019, **58**, 1468–1473.
62 B. Chen, R. Hoffmann, N. W. Ashcroft, J. Badding, E. Xu and V. Crespi, *J. Am. Chem. Soc.*, 2015, **137**, 14373–14386.

